Journal of
Materials Chemistry A

Materials for energy and sustainability

ROYAL SOCIETY
OF CHEMISTRY
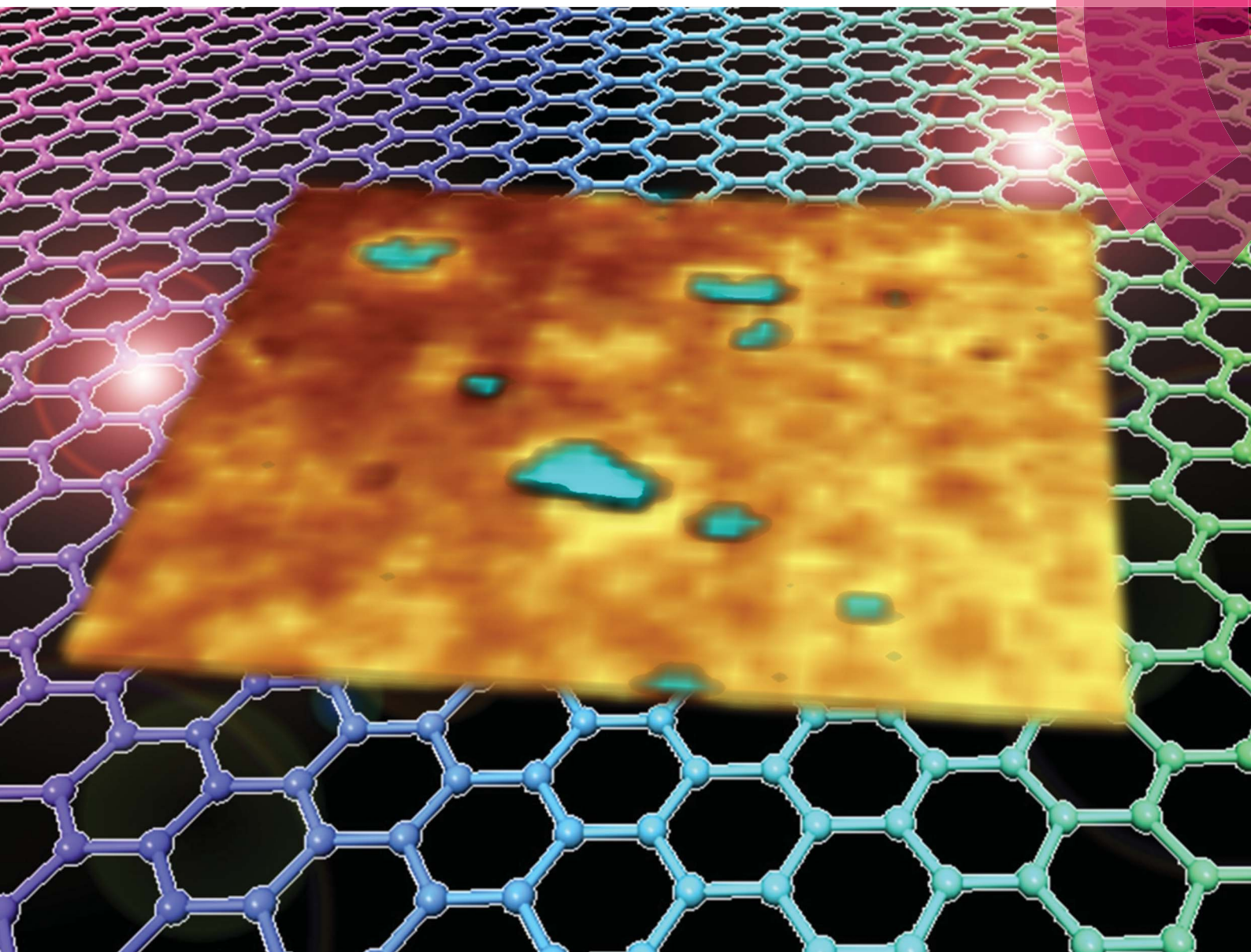
PAPER
Isabella Concina, Federico Rosei, Alberto Vomiero *et al.*
Graphene below the percolation threshold in TiO$_2$ for dye-sensitized solar
cells

PAPER

CrossMark
click for updates

Graphene below the percolation threshold in TiO$_2$ for dye-sensitized solar cells

Kadiatou Therese Dembele,[a] Gurpreet Singh Selopal,[bc] Riccardo Milan,[bc] Charles Trudeau,[d] Daniele Benetti,[a] Afsoon Soudi,[a] Marta Maria Natile,[ef] Giorgio Sberveglieri,[bc] Sylvain Cloutier,[d] Isabella Concina,*[bc] Federico Rosei*[a] and Alberto Vomiero†*[c]

We demonstrate a fast and large area-scalable methodology for the fabrication of efficient dye sensitized solar cells (DSSCs) by simple addition of graphene micro-platelets to TiO$_2$ nanoparticulate paste (graphene concentration in the range of 0 to 1.5 wt%). Two dimensional (2D) Raman spectroscopy, scanning electron microscopy (SEM) and atomic force microscopy (AFM) confirm the presence of graphene after 500 °C annealing for 30 minutes. Graphene addition increases the photocurrent density from 12.4 mA cm^{-2} in bare TiO$_2$ to 17.1 mA cm^{-2} in an optimized photoanode (0.01 wt% graphene, much lower than those reported in previous studies), boosting the photoconversion efficiency (PCE) from 6.3 up to 8.8%. The investigation of the 2D graphene distribution showed that an optimized concentration is far below the percolation threshold, indicating that the increased PCE does not rely on the formation of an interconnected network, as inferred by prior investigations, but rather, on increased charge injection from TiO$_2$ to the front electrode. These results give insights into the role of graphene in improving the functional properties of DSSCs and identifying a straightforward methodology for the synthesis of new photoanodes.

Introduction

Dye sensitized solar cells (DSSCs)[1–3] have been studied extensively during the last decade in the context of new generation photovoltaic devices, due to their unique features like low cost, simple and inexpensive processes and straightforward scalability. An impressive 10% photoconversion efficiency was obtained by Gratzel and co-workers by using a TiO$_2$ mesoporous anatase film sensitized by the so-called N719 dye.[4] They are now in a renaissance period,[5] prompted by recent major advances in the design of new dyes and electrolytes, which can boost the photoconversion efficiency above 12%.[6]

One of the major bottlenecks for further improvement of the photoconversion efficiency is the inhibition of charge recombination, which competes with transport of photogenerated

[a]*INRS-EMT, 1650 Boul. Lionel Boulet, J3X 1S2 Varennes, QC, Canada. E-mail: rosei@emt.inrs.ca*

[b]*SENSOR Lab, Department of Information Engineering, University of Brescia, Via Valotti 9, 25133 Brescia, Italy. E-mail: isabella.concina@unibs.it*
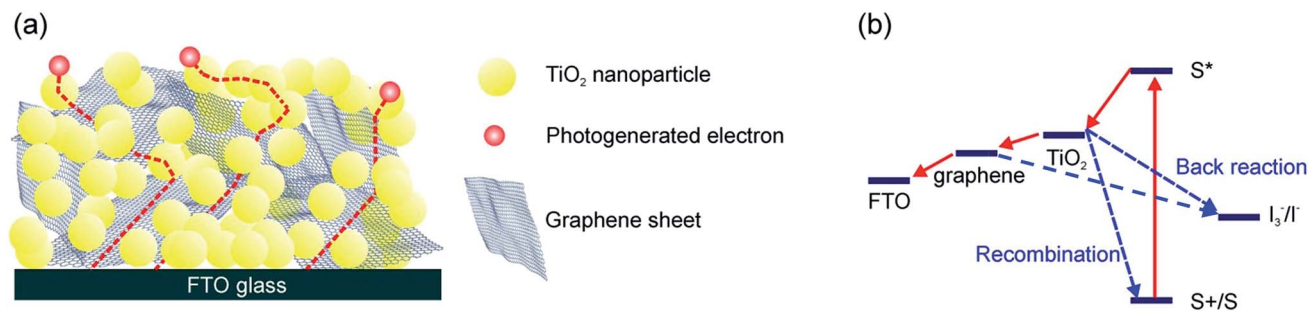
[c]*CNR-INO SENSOR Lab, Via Branze, 45, 25123 BRESCIA, Italy*

[d]*Département de Génie Électrique, École de technologie supérieure, 1100 rue Notre-Dame Ouest, H3C 1K3 Montréal, QC, Canada*

[e]*CNR-IENI, via F. Marzolo 1, 35131 Padova, Italy*

[f]*Department of Chemical Sciences, University of Padova, via F. Marzolo 1, 35131 Padova, Italy*

† Present address: Luleå University of Technology, 971 98 Luleå, Sweden. Email: alberto.vomiero@ltu.se

electrons across the TiO$_2$ nanoparticle network. Various strategies have been recently proposed to increase charge collection, such as *e.g.* the exploitation of highly conducting one-dimensional (1D) oxide nanostructures (nanotubes,[7–10] nanowires,[11,12] and composite systems[13,14]) or hierarchically assembled photoanodes.[15–17]

Carbon-based materials (1D carbon nanotubes (CNTs))[18–20] and, more recently, 2D graphene[21,22] were proposed as additives for conventional TiO$_2$ photoanodes to increase the electron mobility, due to their exceptional electronic properties.

In particular, graphene microplatelets have high electrical conductivity and high transparency (absorbance 2.3% per monolayer in the visible range). Since it extends in two dimensions, addition of a small amount of graphene to the TiO$_2$ anode is claimed[22] to create a 3D percolating network of a highly conducting and almost transparent material perfectly matching the electron band alignment between the TiO$_2$ and the fluorine-doped tin oxide (FTO) conducting glass (see Scheme 1), offering an efficient pathway for fast collection of photogenerated electrons.

The few existing studies on the application of graphene in DSSC photoanodes[23,24] reported a limited increase in the overall photoconversion efficiency (PCE).[25–31] Another recently exploited strategy relies on the addition of tin oxide nanosheets to TiO$_2$ anatase nanopowder,[32] featuring quite a high PCE (8.25%).

A major issue with previous work is the extremely high graphene concentration inserted into the photoanode, which does not allow full exploitation of this strategy, similar to studies

Scheme 1 (a) Schematic illustration of the concept of improved charge collection in a photoanode based on a composite system with a 3D graphene network embedded in a TiO_2 mesoporous structure. (b) Electronic band diagram of the DSSC illustrating the beneficial effect of the insertion of graphene in boosting electron injection from TiO_2 nanoparticles to the collecting FTO.

reporting the addition of CNTs. In some cases, graphene was added to TiO_2 in the form of graphene oxide and then reduced, highly affecting the time needed for photoanode preparation. For instance, 24 h are needed in the case of ref. 22, only for the step of reduction of graphene oxide. Such a long time is too slow in view of its practical exploitation and scale-up.

Herein we demonstrate a simple, very fast and highly reproducible methodology for incorporating low quantities of graphene microplatelets into the traditional photoanode of a DSSC. We applied a straightforward preparation method, only including tape casting and sintering processes: we did not apply any surface treatment (*e.g.* $TiCl_4$ bath and/or vacuum-based plasma cleaning), which of course significantly increases the functional properties of DSSCs, but which is rather unlikely to be applied on a large scale for cheap and massive production.

Experimental

Materials

Transparent TiO_2 paste (20 nm diameter anatase nanoparticles, DSL 18NR-T) and a high performance electrolyte (EL-HPE) were purchased from Dyesol; the N719 dye was purchased from Sigma Aldrich and graphene microplatelets were purchased from Cheaptubes. The redox electrolyte was composed of 0.1 M LiI, 0.05 M I_2, 0.6 M 1,2-dimethyl-3-*n*-propylimidazolium iodide, and 0.5 M 4-*tert*-butylpyridine dissolved in acetonitrile. All chemicals were purchased from Sigma-Aldrich and used without any further purification.

Photoanode preparation and characterization

An ethanol suspension of graphene platelets was prepared and sonicated for 3 hours to obtain a good dispersion of graphene in ethanol. A precise amount was then mixed with a known weight of TiO_2 paste, to obtain a mixed composite, containing fixed percentages of graphene (from 0.005%, up to 1.5% in weight (wt)). The minimum graphene concentration achievable in a controlled and reproducible way was 0.005%, which represents the inferior limit of the investigated graphene concentration range in this work. A pure TiO_2 photoanode without graphene addition was also considered as a benchmark.

TiO_2–graphene and the pure TiO_2 paste were tape cast on FTO glass. A drying process was carried out for 15 minutes at ambient atmosphere and temperature and then for 6 minutes at 150 °C. Subsequently the photoanodes were annealed at 500 °C for 30 minutes in an ambient atmosphere. The final percentage of graphene in the TiO_2 photoanode was estimated taking into account the photoanode weight after annealing. The weight loss of TiO_2 paste after annealing was evaluated by gravimetry and was found to be 80% of the original weight before sintering.

After annealing, the photoanodes were characterized before dye sensitization through UV-Vis absorbance, scanning electron microscopy (SEM), X-ray diffraction (XRD), Raman spectroscopy and X-ray Photoelectron Spectroscopy (XPS).

The photoanodes were dye-sensitized by immersion into 0.5 mM ethanol solution of the commercial Ru-based complex molecular N719 dye for 24 hours and then washed with ethanol to remove any excess of unabsorbed dye molecules.

Dye loading was quantitatively evaluated using UV-Vis spectrophotometry after complete removal of the dye from the photoanode with 0.1 M aqueous NaOH.

Solar cell fabrication and testing

The DSSCs were fabricated by using the I_3^-/I^- redox couple electrolyte, platinized FTO glass as the counter-electrode (a 5 nm thin film of Pt on FTO by sputtering), with 25 μm thick plastic spacers between the photoanode and the Pt counter electrode.

The current–voltage characteristics of the fabricated cells were measured by using a Keithley 2400 SourceMeter under simulated sunlight using an ABET2000 solar simulator at AM 1.5G (100 mW cm^{-2}) calibrated using a reference silicon cell and mechanical filters. During measurements, the cell was masked with a square mask and the irradiated area was 0.25 cm^2. The TiO_2 layer, square in shape, has dimensions slightly larger than the mask, for a typical active area of around 0.27–0.30 cm^2. At least three cells were tested for each concentration, to evaluate the repeatability of the fabrication procedure and the accuracy of the results.

Electrochemical impedance spectroscopy (EIS) was carried out both in the dark and under simulated sunlight using a SOLARTRON 1260 A Impedance/Gain-Phase Analyzer, with an

AC signal of 20 mV in amplitude, in the frequency range between 100 mHz and 300 kHz. The applied bias during measurements in the dark was between 0 V and 100 mV above the open-circuit voltage of the solar cell under illumination. The applied bias during measurements under simulated sunlight (AM 1.5G 100 mW cm^{-2}) was equal to the V_{oc}. All the samples were measured inside a Faraday cage.

Results and discussion

The first aim of our investigation is the characterization of the spatial distribution of graphene inside the TiO$_2$ network. Direct imaging of graphene sheets and/or CNTs dispersed in a mesoporous TiO$_2$ film is not trivial, since they tend to be conformally coated by the NPs. In ref. 20 and 22, CNTs and graphene are detected through the indirect effect of the formation of extended cracks and/or increase of the porosity of the electrode. Graphene is directly detected[22] only at very high concentrations

(0.6 wt%), when the volume occupied by graphene is a significant fraction of the total volume.

For this reason, we used three complementary techniques, namely 2D Raman spectroscopy, SEM and AFM, to confirm the presence of graphene and to estimate its distribution.

The TiO$_2$ composite systems at different graphene contents were analysed using 2D Raman spectroscopy after sintering (Fig. 1 and 2). Fig. 1(a) shows the Raman spectrum averaged over a 50 μm × 50 μm area of the sample containing 0.010 wt% graphene.[33,34] The D and G bands of graphene at around 1350 and 1582 cm^{-1}, which can be attributed to graphene defects, a disorder-induced mode, and in-plane E$_{2g}$ zone-centre mode, respectively, are present in all the analysed samples, even at the lowest graphene concentrations (0.010 wt%). This result confirms the presence of graphene in the nanocomposite, which preserves its original structure after the high temperature annealing of the film. The relative intensity of the D and G bands varies over the sample, as clearly demonstrated in Fig. 1(b)–(f). We were able to map the 2D distribution of the D and G bands and their relative intensity. The D band, related to graphene defects, is more intense at the edge of the platelets, in which a higher amount of defects is expected, while the G band, which is a Raman signature of sp^2 carbon bonds, is more intense in the centre of the platelet.[35]

D and G band mapping over a statistically relevant area of the samples (50 μm × 50 μm) allows direct imaging of graphene distribution on samples at different graphene contents (Fig. 2). On bare TiO$_2$ films, no graphene platelets are detected, while the number of platelets and their density increase with the
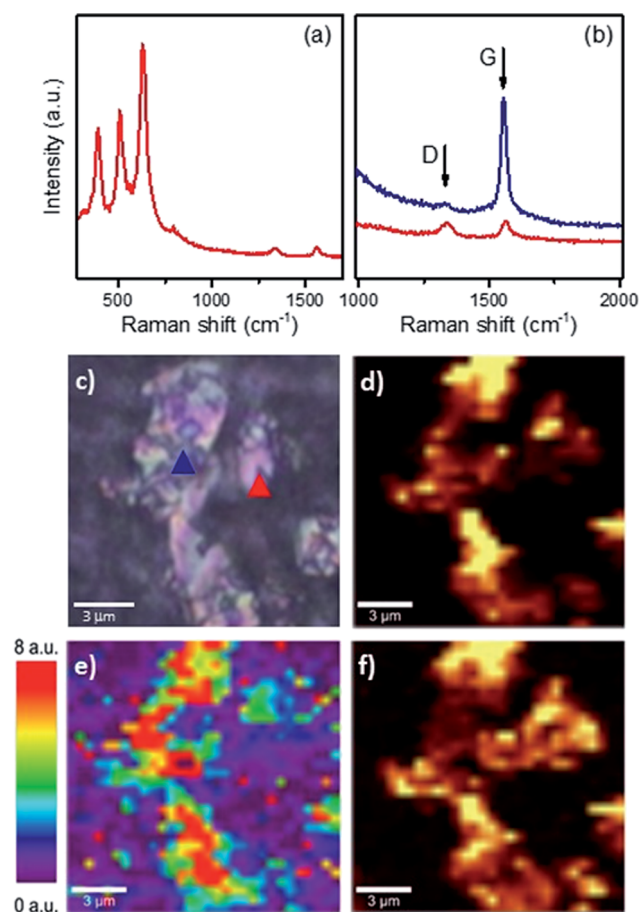

Fig. 1 (a) Raman spectrum averaged on a 50 μm × 50 μm area of the sample containing 0.010 wt% graphene. (b) Raman spectra of two selected regions of the sample reported in (c) (colours of the lines correspond to the colours of the triangles in (c)). (c to f) 2D mapping of graphene in the sample containing 1.5 wt% graphene. (c) Optical imaging of the analysed sample. (d and f) 2D mapping of D and G Raman band intensities. (e) 2D mapping of the relative intensity of the signal of the G band over the D band.
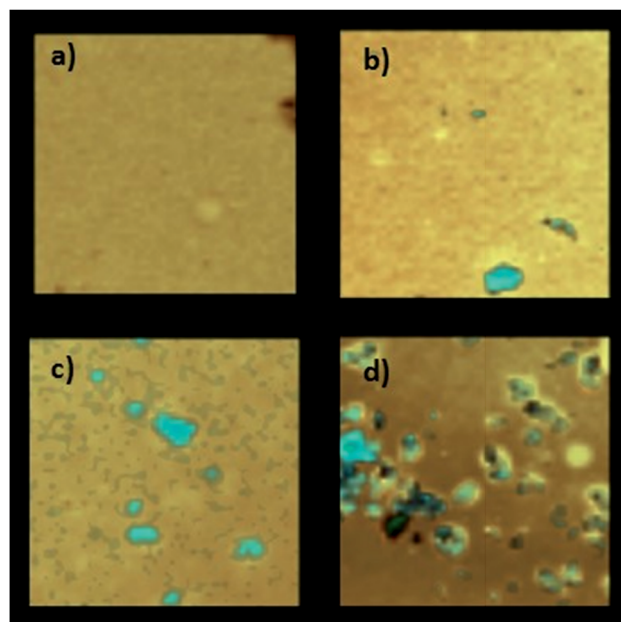

Fig. 2 2D mapping of graphene platelets based on the G band at 1550 cm^{-1} for identification of graphene (azure scale) and on the band at 630 cm^{-1} for TiO$_2$ (yellow scale). The scanned area is 50 μm × 50 μm. The samples correspond to four different graphene concentrations, namely (a) 0 wt% graphene; (b) 0.010 wt% graphene; (c) 0.075 wt% graphene; (d) 1.5 wt% graphene.
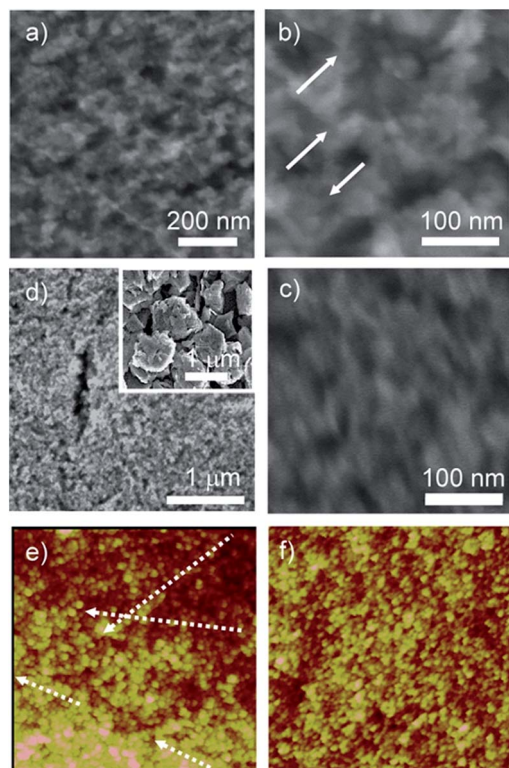
Fig. 3 SEM and AFM images of TiO$_2$ mesoporous films with and without addition of 0.15 wt% graphene (scanned area in AFM: 4 × 4 μm^2). (a, b, d and e) composite sample; (c and f) pure TiO$_2$ layer. In (a, b and e), the graphene sheets are visible as straight lines favouring ordered alignment of TiO$_2$ NPs. In (b), the solid arrows mark three crossing points between different graphene sheets. In (e), the dotted lines run parallel to graphene edges (other edges are visible, not highlighted by arrows). In (d), formation of cracks as a consequence of addition of the high concentration of graphene is visible. The inset shows graphene platelets before insertion into the TiO$_2$ host.

Fig. 4 Ti 2p and O 1s XP peak spectra. (The spectra are normalized to their maximum value.)

increase of the nominal graphene concentration. The lateral size of platelets (certified by the Supplier) is below 2 μm. Raman mapping indicates formation of aggregates up to 8 μm in size, clearly indicating platelet aggregation during the preparation of the photoanodes. At least up to 0.020 wt%, graphene distribution is below the percolation threshold, and we can exclude the formation of a percolating network inside the mesoporous film. This will be important to give an exhaustive explanation of the functional properties of the operating solar cells.

In the present study, we performed direct imaging using SEM and AFM in samples containing 0.15 wt% (Fig. 3), in which extended graphene sheets (lateral dimensions in the micrometre scale) forming a connected 2D network are clearly visible. The formation of a percolation network at 0.15 wt% is in agreement with previous results obtained by 2D Raman spectroscopy. These observations confirm the possibility of integrating graphene sheets in the final photoanode.

In the low magnification image (Fig. 3(d)), the formation of small but extended cracks is visible. The cracks are not present in samples with graphene concentration up to 0.075% (not reported), while their number and extension increases with increasing graphene content.
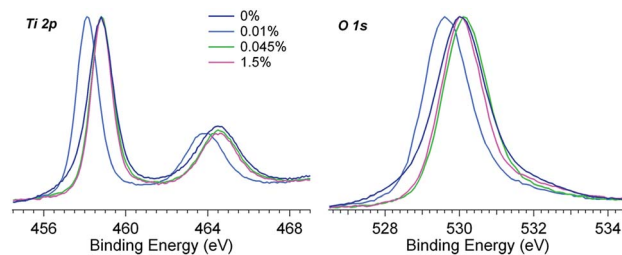
The surface structure of the TiO$_2$ composite systems with different graphene contents was also investigated by using XPS analysis (Fig. 4). Interestingly, the binding energies of Ti 2p for the sample containing 0.010 wt% graphene shift to lower values (458.1 and 463.8 eV) compared with the corresponding values of pure TiO$_2$ (458.9 and 464.6 eV). The same trend is also observed for the O 1s core level (529.7 eV and 530.1 eV, respectively for the composite with 0.01 wt% of graphene and pure TiO$_2$). This shift, not evident in the samples characterized by the higher graphene content, seems to suggest an intimate interaction between graphene and Ti(IV) in TiO$_2$ nanocrystals. This datum, together with the Raman findings, seems to suggest a preference of graphene platelets to stick together, in the case of high concentration, rather than to interact with TiO$_2$. It is however interesting to note that previous literature dealing with the integration of graphene in DSSC photoanodes did not report information on this point. Wang and co-workers[36] deeply investigated carbon nanosheet/1D TiO$_2$ nanostructures (exploited as photocatalysts) by means of TGA-DTA, FTIR and XRD, but no information could be inferred about the nature of the interaction between the two elements. A more detailed study of this interaction would deserve a dedicated investigation, which is beyond the aim of the present work.

The optical properties and dye loading of the films are reported in Fig. 5. The addition of small amounts of graphene (up to 0.03 wt%) does not significantly affect the transparency of the layer, which remains above 85%, the same as the pure NP film. Above 0.06 wt% graphene, the addition leads to a homogeneous increase of absorption in the visible range, which can negatively affect the photovoltaic properties of the device, because part of the radiation is absorbed by graphene, without generating free electrons to be collected. Dye loading is also affected by the presence of graphene, as is clearly visible in Fig. 5(b). Dye loading linearly increases with graphene concentration, most probably due to direct dye attachment to graphene platelets.[21,25]

At first glance, an increased dye uptake would be beneficial for the photovoltaic properties of the device, because an increased optical density of the material can boost photon collection and photoelectron generation. However, the functional characterization of the solar cells demonstrates that increased dye loading has a minor effect in terms of improving device performance, most probably because this beneficial effect is neutralized by the detrimental process induced into the solar cell by the excess of graphene, as explained in the discussion of the experimental results.
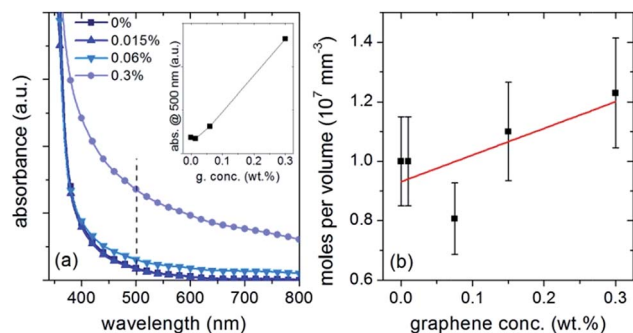
This journal is © The Royal Society of Chemistry 2015

J. Mater. Chem. A, 2015, **3**, 2580–2588 | **2583**

Fig. 5 (a) UV-Vis absorbance spectra normalized to the film thickness of the TiO_2−graphene system for selected samples at different graphene concentrations in the range of 350−800 nm. Inset in (a): absorbance at 500 nm (dashed line in (a)) as a function of graphene concentration. (b) Dye loading vs. graphene concentration. The red line is the linear fit of the experimental data.

The results of current density–voltage measurements on DSSCs under simulated sunlight at one sun (AM 1.5G, 100 mW cm^{-2}) are reported in Fig. 6 and Table 1, including the open circuit photovoltage (V_{oc}), the short circuit photocurrent (J_{sc}), the fill factor (FF) and the photoconversion efficiency (PCE). The lowest graphene concentration (0.005%) does not significantly alter cell parameters, which do not vary compared to pure TiO_2.
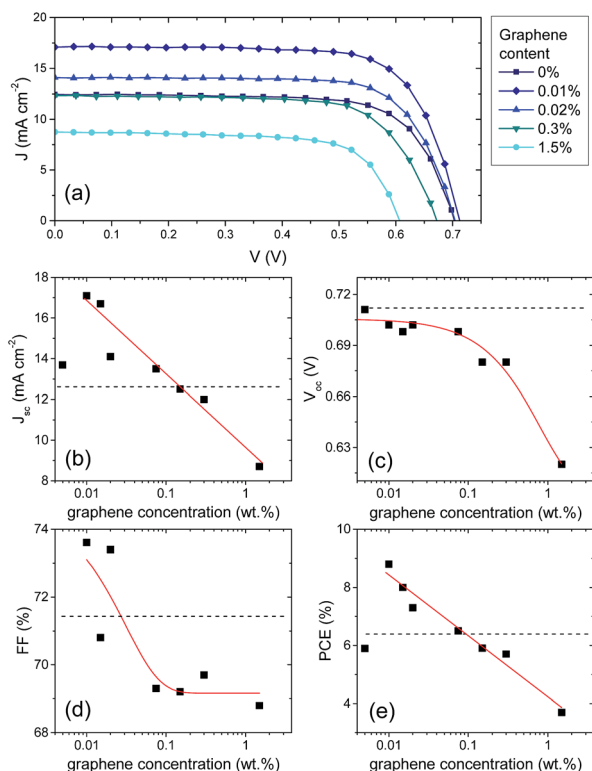

Fig. 6 (a) Current density−voltage curves of solar cells at four different graphene concentrations under simulated sunlight (AM 1.5G, 100 mW cm^{-2}). (b to e) Functional properties (J_{sc}, V_{oc}, FF and PCE, respectively) of the solar cells as a function of the graphene content. Red lines are a guide for the eye. The horizontal dashed line represents the value measured for the pure TiO_2 photoanode.

Table 1 Functional properties of DSSCs under 1 sun irradiation (AM 1.5G, 100 mW cm^{-2}) as a function of the graphene content

Graphene (wt%)	J_{sc} (mA cm^{-2})	V_{oc} (V)	FF (%)	PCE (%)
0	12.4	0.717	71.3	6.3
0.005	13.7	0.711	60.4	5.9
0.010	17.1	0.702	73.6	8.8
0.015	16.7	0.698	70.8	8.0
0.020	14.1	0.702	73.4	7.3
0.075	13.5	0.698	69.3	6.5
0.150	12.5	0.680	69.2	5.9
0.300	12.0	0.680	69.7	5.7
1.5	8.7	0.620	68.8	3.7

The presence of graphene in the concentration range 0.010 wt% and 0.075 wt% significantly enhances the J_{sc} with respect to the case of a pure TiO_2 photoanode, while it has less influence on the other cell parameters. The J_{sc} is maximized in the sample with the lowest graphene content (0.010 wt%) and then exponentially decreases as a function of graphene addition: 0.15 wt% of graphene results in a J_{sc} almost equal to the sample of pure TiO_2. V_{oc} shows a very different trend: it monotonically decreases with the addition of graphene and is systematically lower than pure TiO_2.

This behaviour can be explained in terms of the band alignment in the composite system illustrated in Scheme 1b. A possible explanation for this behaviour is that increasing the graphene concentration downshifts the conduction band of the composite TiO_2–graphene system with respect to pure TiO_2, resulting in a systematic decrease of the V_{oc} of the final device. As expected, such a downshifting effect increases with the increasing amount of graphene in the layer. Another possible reason is the intimate contact between graphene and the electrolyte, which induces strong electron transfer from the conducting graphene to the electrolyte, reducing at the same time V_{oc} and J_{sc}, as observed experimentally.

The increase in J_{sc} is mainly responsible for the drastic boost of PCE in these samples. At graphene concentrations 0.010 wt% and 0.075 wt%, the PCE is higher than for pure TiO_2, with the maximum increase at the minimum graphene concentration, resulting in PCE as high as 8.8%, with an increase of around 40% with respect to pure TiO_2 (6.3%). This is unprecedented with respect to previously reported results in the literature on TiO_2–graphene systems. These results directly testify that graphene addition is highly effective in improving the performance of DSSCs.

A rational understanding of the functional properties of the solar cells was obtained by using EIS. We measure two relevant parameters describing the photoelectron transfer processes in a photoelectrochemical system, i.e. the chemical capacitance (C_μ) and the recombination resistance (R_{REC}) as a function of the applied bias, to understand the role of graphene at the oxide–electrolyte interface. EIS results of four selected samples at different graphene concentrations are reported in Fig. 7. The sample with the lowest graphene concentration (0.005 wt%, not reported) exhibits almost the same trends and values for C_μ and

R_{REC} as the pure TiO$_2$, suggesting that graphene is not effective below a certain threshold. In the bias interval 400–900 mV, the chemical capacitance increases, as expected. Higher values for C_μ are obtained for samples with higher graphene concentration: at 600 mV bias, close to V_{oc}, C_μ in the sample with the highest graphene concentration is four times larger than in pure TiO$_2$. This behaviour can be related to the increased effective surface area of the photoanode in contact with the electrolyte.[37] In the analysis of the recombination resistance, the cell without graphene presents the highest R_{REC} compared to all the other photoanodes.

A large surface exposed to the electrolyte creates a preferential pathway for the recombination of photogenerated charges for the oxide to the electrolyte (low recombination resistance R_{REC}) reducing the functional performance of the cell.

Based on the relationship between C_μ and the position of the conduction band of the photoanode E_C,[38,39] the trend reported in Fig. 7(b) confirms the downward shift of the conduction band with increasing graphene content.

Another clear effect of the presence of graphene is visible in the high frequency semicircle in the Nyquist diagram reported in Fig. 7(a). The real part of this element represents the response of the Pt–electrolyte interface at the counter electrode and the FTO–oxide interface.[40] The addition of graphene reduces the diameter of the semicircle. Since the counter electrode is the same for all samples, the reduced resistance can be attributed to the enhancement of contact between FTO and oxide, thanks to the presence of graphene, which favours charge injection from the photoanode to the FTO.

We repeated EIS measurements under simulated sunlight irradiation around the V_{oc} of each cell. The Bode phase plot of selected cells is reported in Fig. 7(d). The electron lifetime was determined from the main peak at minimum phase angle (in the 10–100 Hz range) according to eqn (1):[41]

$$\tau = \frac{1}{2\pi f_{peak}} \quad (1)$$

where f_{peak} is the peak frequency in the Bode plot.

The incorporation of small quantities of graphene (0.01 wt%), corresponding to the best operating device, increases the electron lifetime compared to bare TiO$_2$. However, adding a very high graphene concentration (1.5 wt%) leads to a catastrophic reduction of electron lifetime, as clearly testified by the large shift in the Bode plot, confirming the results obtained from EIS in the dark, i.e. very low recombination resistance and chemical capacitance, leading to a preferential path for electron transfer from the photoanode to the electrolyte.

These results are confirmed by transient photovoltage decay. The electron lifetime τ_e calculated from transient photovoltage decay according to eqn (2) (ref. 42) is reported in Fig. 8 for DSSCs at different graphene concentration values.

$$\tau_e = \frac{k_B T}{e} \left(\frac{dV_{oc}}{dt} \right)^{-1} \quad (2)$$

The largest electron lifetime is found for the 0.01 wt% graphene concentration, in agreement with EIS in the dark and under light. The addition of a large amount of graphene (1.5 wt%) confirms the very short electron lifetime, induced by very fast electron transfer from the photoanode to the electrolyte, resulting in very large electron recombination, which negatively affects the cell performance. On this basis, we can conclude that the addition of moderate quantities of graphene highly improves the PCE, but an excessive amount of graphene induces an electrochemical short circuit, in which electrons are massively injected into the electrolyte and no longer collected at the anode.

However, the mechanism at the origin of the observed improved performance upon graphene addition is still debated. At least three components should be considered here: (i) the increased dye loading at higher graphene concentration; (ii) the increased charge collection and reduced recombination upon
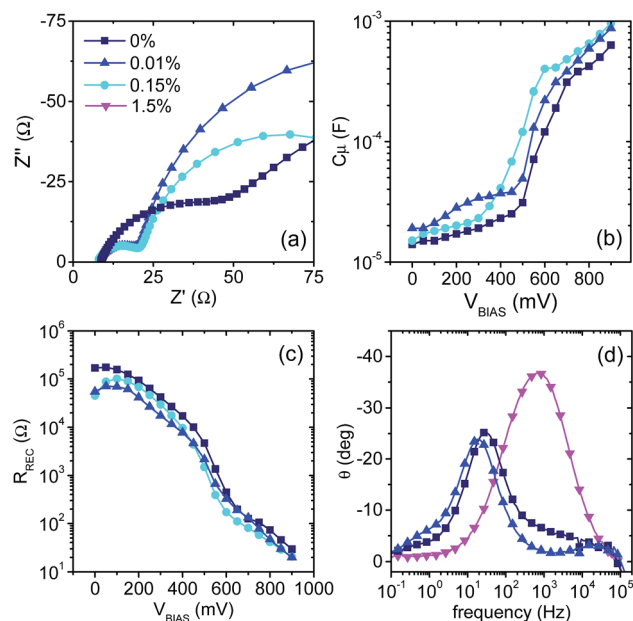

Fig. 7 EIS results of DSSCs at different graphene concentrations. (a) Nyquist plots in the dark at bias equal to V_{oc} of cells under 1 sun irradiation; (b) chemical capacitance and (c) recombination resistance from EIS measurements in the dark; (d) Bode plots under simulated sunlight at bias equal to the V_{oc} of cells under 1 sun irradiation.
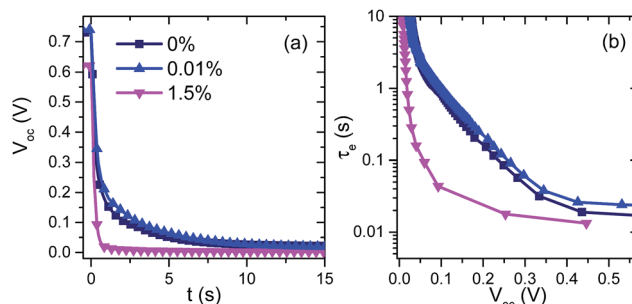

Fig. 8 (a) Transient photovoltage decay and (b) electron lifetime for DSSCs with the addition of different graphene concentrations.

addition of small graphene concentrations; (iii) the mechanical defects (cracks and voids induced by the presence of graphene at high concentrations).

Previously, Kamat and co-workers[43] reached opposite conclusions. Working on a composite TiO_2–CNT system, they observed a significant increase in J_{sc}, but the strong V_{oc} decrease that they attributed to the downshift of the conduction band was much more pronounced than in the present work, so that the PCE did not increase.

However, in their investigation, a much higher CNT concentration was used (the photoanode was a bundle of single walled CNTs decorated with TiO_2 nanoparticles) and the V_{oc} decrease was significantly more pronounced (more than 60 mV over an original V_{oc} of 320 mV, while in our study the maximum decrease is 37 mV over 717 mV V_{oc}). Results closer to the ones reported here are collected in Fig. 9, where our results are compared with previous data from the literature on TiO_2–graphene composites, that highlight the limited photoconversion efficiency obtained in previous studies. Bisquert and co-workers attributed the increased PCE to the enhanced light absorption as a direct consequence of increased dye loading.[21] On the other hand, Wang and co-workers[22] pointed out the beneficial role of graphene in increasing the transport properties of the photoanode towards better performances. In the present study, no increase in dye loading was found in the solar cell with best performance, indicating a limited role of dye loading in boosting the PCE.

A 15% and 25% increase in PCE was obtained for the composite photoanodes in ref. 25 and 26, up to 6.86% and 5.77% PCE, respectively. These values are much lower than ours, both in terms of relative increase and maximum PCE (40% and 8.8%, respectively, in the present study). Our results suggest that the graphene concentration is the key parameter that plays a critical role in optimizing the performance of DSSCs. In previous work,[22] much higher concentrations of graphene were used, which are far above the optimal ones we

identified to maximize the PCE. Another fundamental difference relies on interpreting the role of graphene. Previous literature suggested that graphene addition leads to the formation of a 3D percolating network, which increases charge transport inside the photoanode. We clearly demonstrated that the maximum PCE corresponds to the graphene concentration far below the percolation threshold, indicating that several effects are responsible for increased efficiency (intimate contact TiO_2–graphene–electrolyte, increased specific surface, favoured charge injection from the TiO_2 to the FTO), but not the formation of a conducting network, which could reduce electron recombination.

As soon as the graphene concentration increases, the mechanical deficiencies induced by the tightly entangled graphene sheets severely affect the mesoporous structure of the photoanode, and the downshift of the conduction band of the hybrid photoanode simultaneously induces a significant lowering of V_{oc}, leading to a drastic decrease in PCE. In addition, at high graphene concentrations, direct absorption of light by graphene is not negligible, reducing the solar radiation available for exciton generation. Finally, the cracks formed in the highly loaded samples represent a severe obstacle for a properly operating system, since they introduce macroscopic fractures that limit direct paths for fast and efficient electron collection. Similar behaviour was found in CNT-based photoanodes at CNT concentrations comparable to the ones found for graphene.[44]

Conclusions

In conclusion, we have demonstrated a fast and highly reproducible methodology to fabricate DSSCs by simple addition of graphene nanoplatelets into a commercial TiO_2 paste. A photoconversion efficiency as high as 8.8% was achieved, which is far above previous results on similar photoanodes based on graphene–TiO_2 composites. The role of graphene is to boost electron injection from the photoanode to the front contact, highly increasing the collection of photogenerated charges and reducing charge recombination. Compared to similar literature on the topic, we demonstrated that the optimum graphene concentration is very low, around 0.01 wt%, and is well below the percolation threshold. This finding is particularly critical, because previous understanding of the role of graphene in DSSC photoanodes was the formation of a 3D percolation network which boosts charge transport, while we experimentally demonstrated that excess graphene reduces the open circuit photovoltage and induces a dramatic increase of charge recombination through direct charge transfer from the photoanode to the electrolyte.

In addition, our preparation methodology is very fast and does not rely on dangerous, vacuum-based or environmentally aggressive chemical processes, like the use of acidic baths, plasma treatments, and similar, which are typically used to boost the photoconversion efficiency in standard fabrication procedures of DSSCs.

These results provide a straightforward way to significantly increase the cell efficiency (up to 40% increase for the best
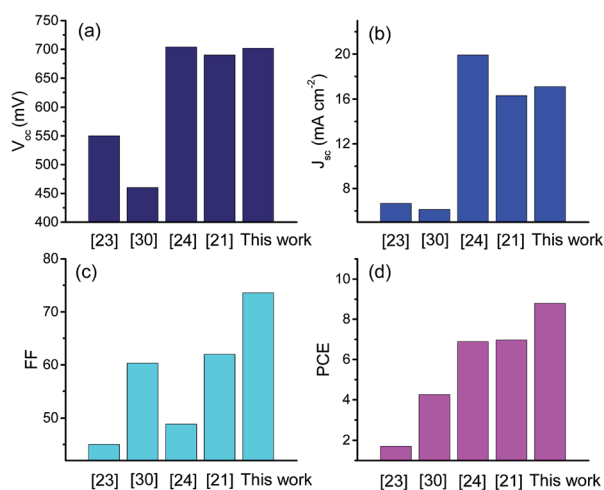

Fig. 9 Functional properties (V_{oc}, J_{sc}, FF and PCE) of the best DSSCs in ref. 22, 24, 25 and 31 as compared to the results of the present manuscript.

2586 | *J. Mater. Chem. A*, 2015, **3**, 2580–2588

This journal is © The Royal Society of Chemistry 2015

operating device) in DSSCs by a scalable and highly reproducible process, representing a major advance for the practical and massive exploitation of this promising technology.

Acknowledgements

Notes and references

1 L. Dai, *Carbon Nanotechnology: Recent developments in chemistry, physics, materials science and devices applications*, Elsevier, Amsterdam, Boston, 2006.

2 B. O' Regan and M. Grätzel, *Nature*, 1991, **353**, 737–740.

3 M. Grätzel, *Curr. Opin. Colloid Interface Sci.*, 1999, **4**, 314–321.

4 M. K. Nazeeruddin, A. Kay, I. Rodicio, R. Humphrybaker, E. Muller, P. Liska, N. Vlachopoulos and M. Gratzel, *J. Am. Chem. Soc.*, 1993, **115**, 6382–6390.

5 B. E. Hardin, H. J. Snaith and M. D. McGehee, *Nat. Photonics*, 2012, **6**, 162–169.

6 A. Yella, H. W. Lee, H. N. Tsao, C. Y. Yi, A. K. Chandiran, M. K. Nazeeruddin, E. W. G. Diau, C. Y. Yeh, S. M. Zakeeruddin and M. Gratzel, *Science*, 2011, **334**, 629–634.

7 V. Galstyan, A. Vomiero, I. Concina, A. Braga, M. Brisotto, E. Bontempi, G. Faglia and G. Sberveglieri, *Small*, 2011, **7**, 2437–2442.

8 A. Vomiero, V. Galstyan, A. Braga, I. Concina, M. Brisotto, E. Bontempi and G. Sberveglieri, *Energy Environ. Sci.*, 2011, **4**, 3408–3413.

9 O. K. Varghese, M. Paulose and C. A. Grimes, *Nat. Nanotechnol.*, 2009, **4**, 592–597.

10 G. K. Mor, K. Shankar, M. Paulose, O. K. Varghese and C. A. Grimes, *Nano Lett.*, 2006, **6**, 215–218.

11 J. B. Baxter and E. S. Aydil, *Appl. Phys. Lett.*, 2005, **86**, 053114.

12 M. Law, L. E. Greene, J. C. Johnson, R. Saykally and P. D. Yang, *Nat. Mater.*, 2005, **4**, 455–459.

13 A. Vomiero, I. Concina, M. Natile, E. Comini, G. Faglia, M. Ferroni, I. Kholmanov and G. Sberveglieri, *Appl. Phys. Lett.*, 2009, **95**, 193104.

14 B. Tan and Y. Y. Wu, *J. Phys. Chem. B*, 2006, **110**, 15932–15938.

15 N. Memarian, I. Concina, A. Braga, S. M. Rozati, A. Vomiero and G. Sberveglieri, *Angew. Chem., Int. Ed.*, 2011, **50**, 12321–12325.

16 Q. F. Zhang, T. R. Chou, B. Russo, S. A. Jenekhe and G. Z. Cao, *Angew. Chem., Int. Ed.*, 2008, **47**, 2402–2406.

17 G. S. Selopal, N. Memarian, R. Milan, I. Concina, G. Sberveglieri and A. Vomiero, *ACS Appl. Mater. Interfaces*, 2014, **6**, 11236–11244.

18 T. Sawatsuk, A. Chindaduang, C. Sae-Kung, S. Pratontep and G. Tumcharern, *Diamond Relat. Mater.*, 2009, **18**, 524–527.

19 K. T. Dembele, R. Nechache, L. Nikolova, A. Vomiero, C. Santato, S. Licoccia and F. Rosei, *J. Power Sources*, 2013, **233**, 93–97.

20 C. Y. Yen, Y. F. Lin, S. H. Liao, C. C. Weng, C. C. Huang, Y. H. Hsiao, C. C. M. Ma, M. C. Chang, H. Shao, M. C. Tsai, C. K. Hsieh, C. H. Tsai and F. B. Weng, *Nanotechnology*, 2008, **19**, 375305.

21 J. Durantini, P. P. Boix, M. Gervaldo, G. M. Morales, L. Otero, J. Bisquert and E. M. Barea, *J. Electroanal. Chem.*, 2012, **683**, 43–46.

22 N. L. Yang, J. Zhai, D. Wang, Y. S. Chen and L. Jiang, *ACS Nano*, 2010, **4**, 887–894.

23 Y. H. Ng, I. V. Lightcap, K. Goodwin, M. Matsumura and P. V. Kamat, *J. Phys. Chem. Lett.*, 2010, **1**, 2222–2227.

24 Y.-B. Tang, C.-S. Lee, J. Xu, Z.-T. Liu, Z.-H. Chen, Z. He, Y.-L. Cao, G. Yuan, H. Song, L. Chen, L. Luo, H.-M. Cheng, W.-J. Zhang, I. Bello and S.-T. Lee, *ACS Nano*, 2010, **4**, 3482–3488.

25 T.-H. Tsai, S.-C. Chiou and S.-M. Chen, *Int. J. Electrochem. Sci.*, 2011, **6**, 3333–3343.

26 J. Fan, S. Liu and J. Yu, *J. Mater. Chem.*, 2012, **22**, 17027–17036.

27 B. Tang and G. Hu, *J. Power Sources*, 2012, **220**, 95–102.

28 B. Tang, G. Hu, H. Gao and Z. Shi, *J. Power Sources*, 2013, **234**, 60–68.

29 W. Shu, Y. Liu, Z. Peng, K. Chen, C. Zhang and W. Chen, *J. Alloys Compd.*, 2013, **563**, 229–233.

30 M.-Y. Yen, M.-C. Hsiao, S.-H. Liao, P.-I. Liu, H.-M. Tsai, C.-C. M. Ma, N.-W. Pu and M.-D. Ger, *Carbon*, 2011, **49**, 10.

31 G. S. Anjusree, A. S. Nair, S. V. Nair and S. Vadukumpully, *RSC Adv.*, 2013, **3**, 12933–12938.

32 S. Yang, Y. Hou, J. Xing, B. Zhang, F. Tian, X. H. Yang and H. G. Yang, *Chem.–Eur. J.*, 2013, **19**, 9366–9370.

33 A. C. Ferrari, *Solid State Commun.*, 2007, **143**, 47–57.

34 D. Graf, F. Molitor, K. Ensslin, C. Stampfer, A. Jungen, C. Hierold and L. Wirtz, *Solid State Commun.*, 2007, **143**, 44–46.

35 C. Casiraghi, A. Hartschuh, H. Qian, S. Piscanec, C. Georgi, A. Fasoli, K. S. Novoselov, D. M. Basko and A. C. Ferrari, *Nano Lett.*, 2009, **9**, 1433–1441.

36 W. Peng, Z. Wang, N. Yoshizawa, H. Hatori, T. Hirotsu and K. Miyazawa, *J. Mater. Chem.*, 2010, **20**, 2424–2431.

37 M. S. Goes, E. Joanni, E. C. Muniz, R. Savu, T. R. Habeck, P. R. Bueno and F. Fabregat-Santiago, *J. Phys. Chem. C*, 2012, **116**, 12415–12421.

38 J. Bisquert, *Phys. Chem. Chem. Phys.*, 2003, **5**, 5360–5364.

39 S. R. Raga, E. M. Barea and F. Fabregat-Santiago, *J. Phys.Chem. Lett.*, 2012, **3**, 1629–1634.

40 F. Fabregat-Santiago, J. Bisquert, E. Palomares, L. Otero, D. Kuang, S. M. Zakeeruddin and M. Gratzel, *J. Phys. Chem. C*, 2007, **111**, 6550–6560.

41 R. Kern, R. Sastrawan, J. Ferber, R. Stangl and J. Luther, *Electrochim. Acta*, 2002, **47**, 4213–4225.

42 A. Zaban, M. Greenshtein and J. Bisquert, *ChemPhysChem*, 2003, **4**, 859–864.

43 P. Brown, K. Takechi and P. V. Kamat, *J. Phys. Chem. C*, 2008, **112**, 4776–4782.

44 K. T. Dembele, G. S. Selopal, C. Soldano, R. Nechache, J. C. Rimada, I. Concina, G. Sberveglieri, F. Rosei and A. Vomiero, *J. Phys. Chem. C*, 2013, **117**, 14510–14517.